ADVANCED FUNCTIONAL MATERIALS

Postfach 10 11 61
69451 Weinheim
Germany
Courier services:
Boschstraße 12
69469 Weinheim
Germany
Tel.: (+49) 6201 606 531
E-mail: afm@wiley.com

WILEY-VCH

Dear Author,

Please correct your galley proofs carefully and return them no more than four days after the page proofs have been received.

Please limit corrections to errors already in the text; cost incurred for any further changes or additions will be charged to the author, unless such changes have been agreed upon by the editor.

The editors reserve the right to publish your article without your corrections if the proofs do not arrive in time.

Note that the author is liable for damages arising from incorrect statements, including misprints.

Please note any queries that require your attention. These are indicated with a Q in the PDF and a question at the end of the document.

Reprints may be ordered by filling out the accompanying form.

Return the reprint order form by e-mail with the corrected proofs to Wiley-VCH: afm@wiley.com

To avoid commonly occurring errors, **please ensure that the following important items are correct** in your proofs (please note that once your article is published online, no further corrections can be made):

- **Names** of all authors present and spelled correctly
- **Addresses** and **postcodes** correct
- **E-mail address** of corresponding author correct (current email address)
- **Funding bodies** included and grant numbers accurate
- **Title** of article OK
- All **figures** included
- **Equations** correct (symbols and sub/superscripts)

Corrections should be made directly in the PDF file using the PDF annotation tools. If you have questions about this, please contact the editorial office. The corrected PDF and any accompanying files should be uploaded to the journal's Editorial Manager site.

Author Query Form

WILEY

Journal ADFM

Article adfm202109593

Dear Author,

During the copyediting of your manuscript the following queries arose.

Please refer to the query reference callout numbers in the page proofs and respond.

Please remember illegible or unclear comments and corrections may delay publication.

Many thanks for your assistance.

Query No.	Description	Remarks
Q-license	Please note that the article can only be published once an appropriate license agreement has been signed. The responsible corresponding author will have received an e-mail invitation to register/log in and sign a license agreement in Wiley Author Services (https://authorservices.wiley.com). The costs of publishing this manuscript OnlineOpen might be covered by one of Wiley's national agreements. To find out more please visit, https://authorservices.wiley.com/authorresources/Journal-Authors/open-access/affiliation-policies-payments/index.html. Eligibility for fee coverage is determined by the affiliation of the responsible corresponding author.	
Q1	Please confirm that forenames/given names (blue) and surnames/family names (vermilion) have been identified correctly.	
Q2	Please define 'FTIR' at its first occurrence in the text.	
Q3	Please check all equations have been correctly typeset.	
Q4	The text 'All authors contributed equally to...version of the manuscript.' given under 'Acknowledgements' section has been set under 'Author Contributions' section. Please verify.	

Please confirm that Funding Information has been identified correctly.

Please confirm that the funding sponsor list below was correctly extracted from your article: that it includes all funders and that the text has been matched to the correct FundRef Registry organization names. If a name was not found in the FundRef registry, it may not be the canonical name form, it may be a program name rather than an organization name, or it may be an organization not yet included in FundRef Registry. If you know of another name form or a parent organization name for a "not found" item on this list below, please share that information.

FundRef Name	FundRef Organization Name
Natural Science Foundation of Jiangsu Province	Natural Science Foundation of Jiangsu Province
Jiangsu Agriculture Science and Technology Innovation Fund	
Jiangsu Specially-Appointed Professor Program	
Advanced Analysis Testing Center, Nanjing Forestry University	

G. Zhou, M.-C. Li,* C. Liu, Q. Wu, C. Mei* 2109593

3D Printed $Ti_3C_2T_x$ MXene/Cellulose Nanofiber Architectures for Solid-State Supercapacitors: Ink Rheology, 3D Printability, and Electrochemical Performance

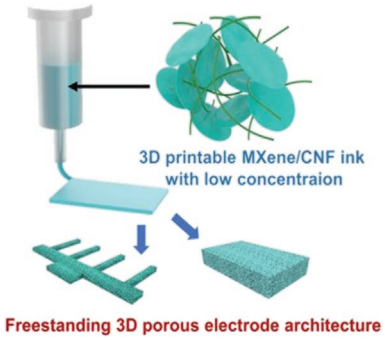

By rationally controlling the dimension and surface chemistry of cellulose nanofibers (CNFs), CNFs are successfully applied as rheology modifiers to formulate viscoelastic, 3D printable MXene-based ink at a low concentration of 8 wt%. The freestanding, hierarchically porous MXene-based electrode architectures can be achieved by 3D printing and freeze-drying approach, which hold the great potential in electrochemical energy storage device.

ADVANCED FUNCTIONAL MATERIALS
www.afm-journal.de

3D Printed $Ti_3C_2T_x$ MXene/Cellulose Nanofiber Architectures for Solid-State Supercapacitors: Ink Rheology, 3D Printability, and Electrochemical Performance

Q1 Guoqiang Zhou, Mei-Chun Li,* Chaozheng Liu, Qinglin Wu, and Changtong Mei*

Direct ink writing technology is capable of using 2D MXene to construct 3D architectures for electrochemical energy storage (EES) devices that are normally difficult to achieve using conventional techniques. However, to meet specific rheological requirements for 3D printing, a large amount of MXene is needed in the ink, resulting in a severe self-restacking structure after drying. Herein, a series of cellulose nanofibers (CNFs) with different morphologies and surface chemistries are applied to enhance the rheology of the MXene-based inks with exceptional 3D printability. Various 3D architectures with superior shape fidelity and geometric accuracy are successfully printed using the optimized hybrid ink at a low solid content, generating self-standing, hierarchically porous structures after being freeze-dried, which improves surface area accessibility, ion transport efficiency, and ultimately, capacitive performance. A solid-state interdigitated symmetrical supercapacitor is further 3D printed, which delivers an areal capacitance of 2.02 F cm^{-2} and an energy density of 101 μWh cm^{-2} at a power density of 0.299 mW cm^{-2}, and maintains a capacitance retention rate of 85% after 5000 cycles. This work demonstrates the integration of 1D CNFs and 2D MXene in 3D printing technology to prepare customized, multiscale, and multidimensional architectures for the next generation of EES devices.

1. Introduction

With rapid evolution of the modern electronics industry, energy storage devices play a crucial role in the future development of portable and smart microsensors, nanorobots, and microelectromechanical systems.[1] The capacity of electrochemical energy storage (EES) device could be improved by the rational design of electrode materials formulation that can maximize surface area accessibility and fast ion transport efficiency.[2] However, constructing novel electrodes with complex 3D structures using advanced manufacturing technology remains an arduous task, apart from the innovation of electrode materials. Direct ink writing (DIW), as an emerging additive manufacturing technique, has a great potential in fabricating 3D electrode architecture for integrating into energy storage systems.[3] The key to 3D printing of stable architectures with high fidelity relies on the formulation of viscoelastic inks with excellent rheological performance. In general, 3D printable inks are required to have shear thinning behavior, high viscoelasticity, and favorable thixotropy.[4] So far, an exciting progress has been made in preparing printable conductive inks utilizing different materials such as graphene,[5] carbon nanotubes,[6] and activated carbon.[3d,7] These inks hold great promise in 3D printing energy storage electrodes.

More recently, MXene, as a family of 2D transition metal carbides, nitrides, and carbonitride, has shown excellent charge storage and transport capabilities due to its high metal conductivity, redox activity, and negatively charged surface.[8] Meanwhile, the surface functional groups (T_x) such as −O, −OH, and −F endow MXene with hydrophilicity, allowing it to effectively form aqueous suspensions for further fabricating into electrodes using various methods such as vacuum filtration,[1d,9] freeze-drying,[10] and spin coating.[11] While these processing approaches hold a great potential in producing MXene-based electrodes for EES devices, there still remain limitations with respect to the electrode architectural design. To realize this challenge, various printing techniques including inkjet printing,[12] screen printing,[13] and extrusion 3D printing (DIW)[2a,14] were applied for constructing MXene electrodes with controllable pattern and architecture.[15] The rheological requirements of ink for those printing methods vary greatly from low-viscosity MXene dispersion for inkjet and screen printing to highly viscous paste for extrusion 3D printing.[16] To date, viscoelastic MXene-based inks with high viscosity have been developed for constructing electrodes with controllable architecture using the DIW.[3d,14] However, these MXene-based inks require extremely high concentrations to achieve printable rheological properties that allow them smooth flow through the narrow printed nozzles while retaining the

G. Zhou, M.-C. Li, C. Liu, C. Mei
Co-Innovation Center of Efficient Processing and Utilization of Forest Resources
College of Materials Science and Engineering
Nanjing Forestry University
Nanjing 210000, China
E-mail: mli@njfu.edu.cn; mei@njfu.edu.cn
Q. Wu
School of Renewable Natural Resources
Louisiana State University AgCenter
Baton Rouge, LA 70803, USA
The ORCID identification number(s) for the author(s) of this article can be found under https://doi.org/10.1002/adfm.202109593.

DOI: 10.1002/adfm.202109593

extruded filaments' shape even after printing multiple layers, which undoubtedly increases the cost-effectiveness of MXene. In addition, analogous with other 2D materials (e.g., graphene oxide), MXene nanosheets are prone to restack through van der Waals forces at high concentrations, resulting in limited surface accessibility, sluggish ionic kinetics, and ultimately ordinary capacitive performance.[10] Therefore, it is of great significance to develop a novel strategy to prepare the viscoelastic, 3D printable MXene-based ink at a low MXene concentration.

Cellulose nanofibers (CNFs) with a high aspect ratio derived from abundant biomass resources hold outstanding adjustable rheological properties after being dispersed in water.[17] A wide range of parameters, including morphology (e.g., rod, fiber, and net), dimension (e.g., width, length and aspect ratio), surface chemistry (e.g., hydrophicility, hydrophobicity, types of functional groups, and density of surface charge), and suspension environments (e.g., concentration, pH, temperature, salinity, and addition of water-soluble polymers) can be employed to control the rheological properties of CNF suspension.[4] Previous studies have demonstrated that the CNF suspension could translate to viscoelastic gel with a strongly entangled network even at low concentrations (e.g., 1.7–2.5 wt%), which can be employed for 3D printing of advanced functional materials.[18] Additionally, CNFs can be also used as a rheology modifier in combination with other functional materials to produce 3D printable gel inks.[19] Hence, it is reasonably hypothesized that low solid content, viscoelastic, 3D printable MXene inks could be realized using CNFs as a rheological modifier via rational design of dimension and surface chemistry of CNFs.

In this contribution, we derived a series of 2,2,6,6-tetramethylpiperidine-1-oxyl (TEMPO)-mediated oxidized CNFs with different diameters and gradient numbers of carboxylate groups on the surface from oil palm woody material via controlling the oxidant content, and applied them as rheology modifiers to formulate viscoelastic, 3D printable MXene-based ink at the low concentration of 8 wt% (**Figure 1**). Subsequent 3D printing of the optimized MXene/CNF inks resulted in customized 3D architectures with highly geometric accuracy. After being freeze-dried, the self-standing, hierarchically porous 3D scaffolds were obtained, which exhibited superior capacitive performance. It is worth noting that the low solid content of 3D printing ink and post freeze-drying route were critical for the formation of hierarchically porous structure, which suppressed the restacking of MXene nanosheets, and improved surface area accessibility within the 3D scaffolds. Furthermore, a solid-state interdigitated symmetric supercapacitor (SSC) device was fabricated based on the 3D printed freeze-dried MXene/CNF pectinate electrodes. It exhibited an areal capacitance of 2.02 F cm^{-2} (25.4 F cm^{-3}) at 1 mA cm^{-2}, and an energy density of 101 μWh cm^{-2} at a power density of 0.299 mW cm^{-2}.

2. Results and Discussion

Oil palm fibers (OPFs) are derived from oil palm woody material, the highest yielding oil crop in the world, which contain 43–65% cellulose, 13–25% lignin, and 17–34% hemicellulose.[20] Accordingly, a series of steps, including hot-water, $NaClO_2$ and

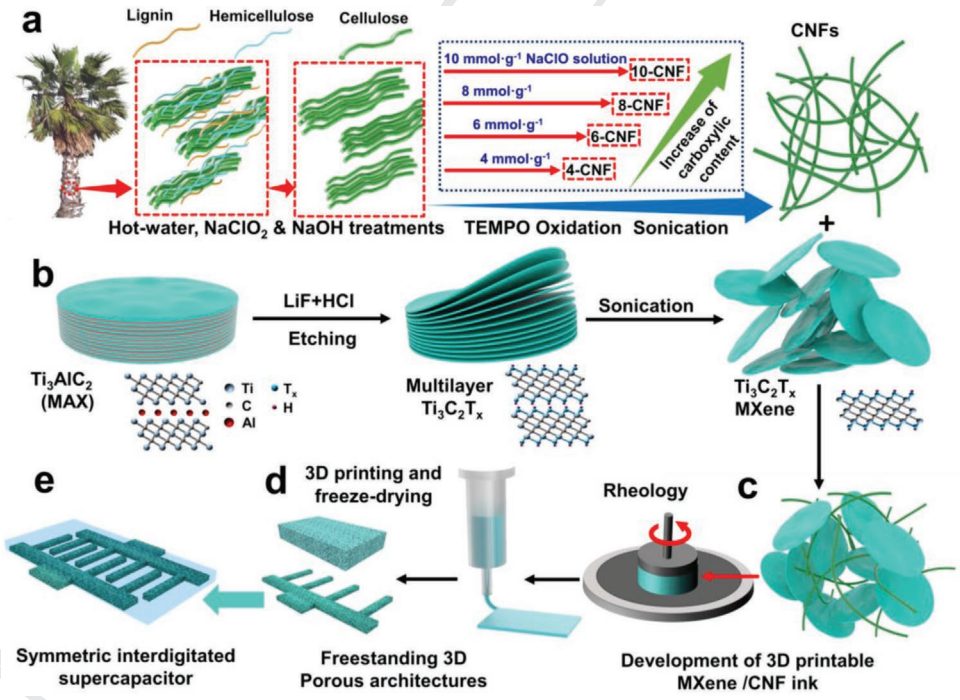

Figure 1. Schematic illustration of the manufacturing strategy for 3D printing of freestanding, hierarchically porous MXene/CNF 3D architecture and symmetric interdigitated supercapacitor: a) Extraction of 1D CNFs from oil palm tree trunk via a series of steps including hot-water, $NaClO_2$ and NaOH treatments, TEMPO oxidation, and sonication. b) Synthesis of 2D MXene nanosheets using the mild etching method, followed by sonication. c) Preparation of MXene/CNF ink and evaluation on its rheological properties. d) 3D printing of ink layer by layer, followed by freeze-drying to produce freestanding 3D porous architectures. e) Fabrication of a solid-state symmetrical supercapacitor using two 3D printed pectinate electrodes.

NaOH treatments, TEMPO-mediated oxidation, and ultrasonication, were designed to isolate CNFs from OPFs (Figure 1a). The hot-water treatment removed most impurities and generated less compact fiber structure compared with neat OPFs (Figure S1a,b, Supporting Information). After the removal of lignin and hemicellulose using 4 wt% $NaClO_2$ solution and 5 wt% NaOH solution, highly pure cellulose fibers were obtained, as shown by the change in fiber morphology (Figure S1c, Supporting Information) and disappearance of characteristic absorption peaks of hemicellulose and lignin at Q2 1247, 1461, 1512 and 1732 cm^{-1} in FTIR spectra (Figure S2, Supporting Information).[21] To achieve nanofibrillation, an efficient TEMPO-mediated oxidation method was applied.[22] During the TEMPO oxidation process, TEMPO radical reacted with NaClO oxidant to generate nitrosonium ions (+N=O) that then in situ oxidized the C6-primary hydroxyl group (−OH) of cellulose to carboxylate group ($-COO^-$) (Figure S3, Supporting Information). This resulted in the presence of electrostatic repulsion between carboxylate groups on the surface of cellulose fibers, which promoted the subsequent nanofibrillation of cellulose using sonication.

The diameter, carboxylate content, and crystallinity of CNFs can be tailored by controlling the amount of NaClO oxidant ranging from 4 to 6, 8, and 10 mmol g^{-1}, producing four types of CNFs referred as 4-CNF, 6-CNF, 8-CNF, and 10-CNF, respectively. As shown in **Figure 2**a–d, the average diameter of CNFs decreases with an increase in the amount of NaClO oxidant, i.e., 11.79, 6.12, 4.56, and 4.27 nm for 4-CNF, 6-CNF, 8-CNF, and 10-CNF, respectively (Figure S4, Supporting Information). Notably, 10-CNF material exhibits the smallest diameter close to that of elementary fibril (i.e., ≈3.5 nm).[23] This is attributed to the highest electrostatic repulsion caused by the increase of carboxylate content, which promoted the degree of nanofibrillation of cellulose.[24] The content of carboxylate group on the surface of CNFs was determined using the conductometric titration method (Figure S5, Supporting Information). As shown in

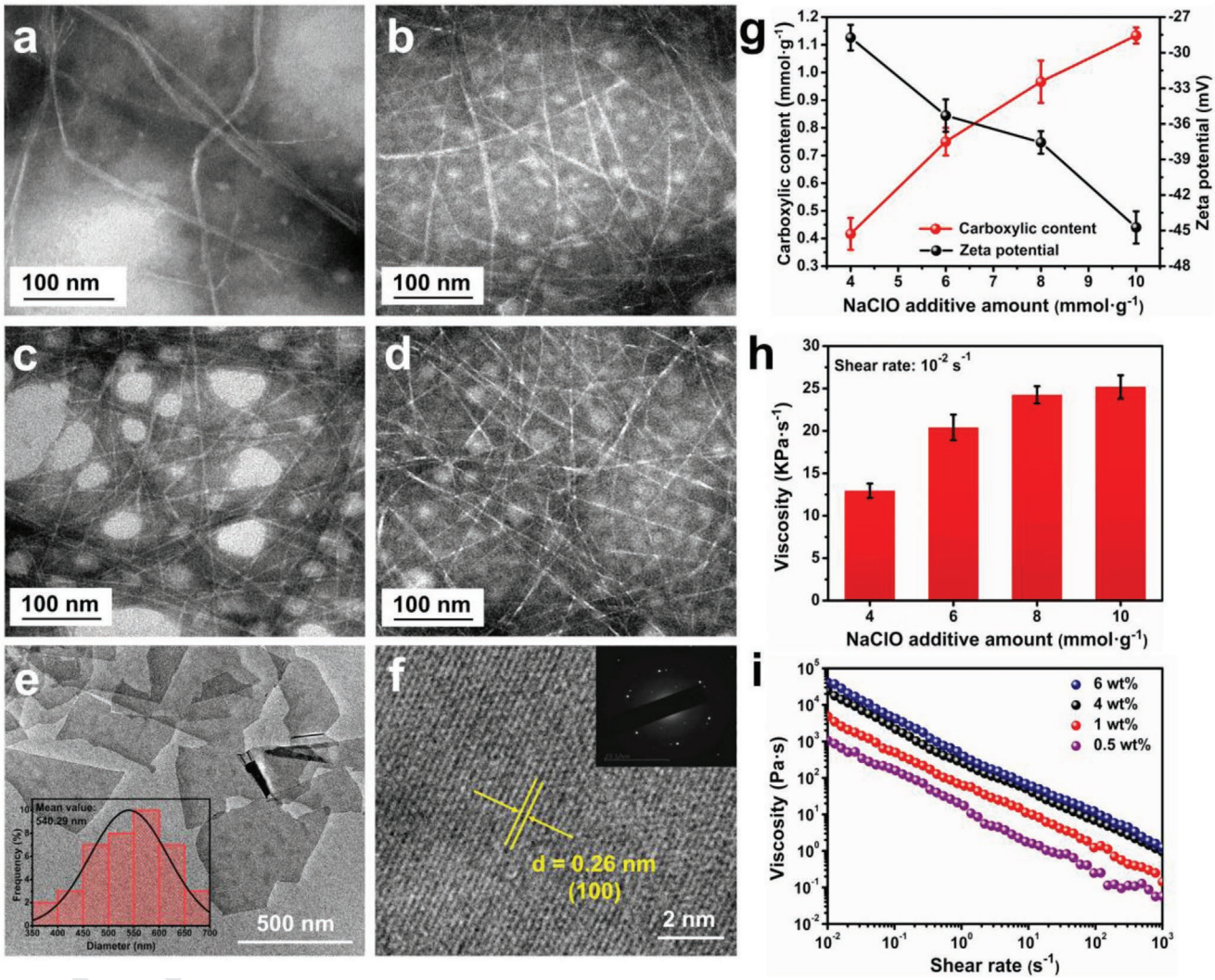

Figure 2. Characterizations of CNFs and MXene: TEM images of a) 4-CNF, b) 6-CNF, c) 8-CNF, d) 10-CNF, and e) MXene. f) HRTEM image of MXene. g) Carboxylate content and Zeta potential of different CNFs. h) Viscosity at a shear rate of 10^{-2} s^{-1} for different CNF suspensions at a concentration of 4 wt%. i) Viscosity of the 8-CNF suspension as a function of shear rate at different concentrations from 0.5 to 6 wt%. Note, in panel (e), inset is the lateral size distribution of MXene. In panel (f), inset is the SAED patterns of MXene.

Figure 2g, the 10-CNF material possesses the highest carboxylate content of 1.13 mmol g^{-1} as well as the lowest zeta potential value of –44.7 mV, which strongly supports our previous explanation that the electrostatic repulsion induced by carboxylated groups is responsible for the diameter of CNFs. In addition, the increase in the amount of NaClO oxidant does not alter the crystalline form, while the crystallinity gradually decreases from 67.30% to 48.54% (Figure S6, Supporting Information). This is caused by the conversion of primary hydroxy groups at the C6 position of cellulose to carboxylate groups by having sodium glucuronosyl units and therefore made the part of crystalline structure of cellulose turn to disordered structure.[25]

The notable variation in diameter, carboxylate content, and crystallinity in turn affect the rheological properties of CNF–water suspensions, therefore enabling CNFs as rheological modifiers to formulate 3D printable MXene ink more effectively. As presented in Figure S7a in the Supporting Information and Figure 2h, the steady-state viscosity of 4 wt% 4-CNF, 6-CNF, 8-CNF, and 10-CNF suspensions at a shear rate of 10^{-2} s^{-1} are 12.95, 20.40, 24.25, and 25.19 kPa s^{-1}, respectively. Similar to the viscosity, the viscoelastic properties of CNF suspensions show an analogous trend, i.e., both storage modulus (G') and loss modulus (G'') increase with an increase in the amount of NaClO (Figure S7b, Supporting Information). These results suggest that the decrease in diameter and increase in carboxylate groups of CNFs are beneficial for the formation of more entangled network, leading to higher viscosity and G'. It is worth noting that when the amount of NaClO is increased from 8 to 10 mmol g^{-1}, the enhancement in viscosity and G' becomes very limited. According to morphological and surface charge analyses (Figure 2a–d,g), the 8-CNF and 10-CNF samples have similar dimension in diameter, but distinctive charge density. These observations reveal that the diameter might have a more pronounced influence on the rheological properties than charge density. Considering the consumption of NaClO and enhanced rheological properties, the 8-CNF material is chosen as the optimized rheological modifier. In addition, the concentration-dependent rheological behavior of 8-CNF suspensions was further evaluated. As shown in Figure 2i, the 8-CNF suspensions possess significant shear-thinning behavior together with a broad range of viscosity from 0.06 to 41 051.78 Pa s^{-1} depending on the concentration of the 8-CNF material applied. For instance, at a low concentration of 0.5 wt%, the viscosity decreases from 1048.04 to 0.06 Pa s^{-1} as the shear rate increases from 10^{-2} to 10^{3} s^{-1}. At a high concentration of 6 wt%, the viscosity decreases from 41 051.78 to 1.26 Pa s^{-1} as the shear rate increases from 10^{-2} to 10^{3} s^{-1}. The highly adjustable viscosity and profound shear-thinning feature make the 8-CNF sample as an excellent rheological modifier to formulate the viscoelastic MXene-based gel for 3D printing.

MXene nanosheets were synthesized by selective etching the Al from the Ti_3AlC_2 in a mixture of LiF and HCl solution, followed by sonication treatment (Figure 1b). Scanning electron microscopy (SEM) images present that the nubbly Ti_3AlC_2 changes to accordion-like multilayered $Ti_3C_2T_x$ after etching treatment due to the removal of the Al layer (Figure S8, Supporting Information). Further sonication leads to the exfoliation of multilayer $Ti_3C_2T_x$, generating individual 2D MXene flakes with a mean diameter of 540.29 nm (Figure 2e). Figure 2f shows the high-resolution transmission electron microscope (HRTEM) images of MXene, in which well-resolved lattice fringes with a typical interplanar spacing of 0.26 nm is observed. Furthermore, the selected area electron diffraction (inset in Figure 2f) exhibits hexagonal symmetry of the planes, which is well in agreement with other studies.[26]

A series of MXene/CNF inks with varied CNF loadings from 0 to 5 and 10 wt% (referred as MXene, MXene/CNF5, and MXene/CNF10 in the following discussion) were developed by mixing MXene and 8-CNF suspensions and concentrating the mixture to a total solid content of 8 wt%. It is worth noting that this solid content is much lower than that of highly concentrated MXene-based inks (i.e., 28.9 wt% and 300 mg mL^{-1}) required for 3D printing.[14b,27] In addition, achieving homogenous dispersion of CNFs and MXene in the hybrid ink is critically important for the formation of viscoelastic gel for 3D printing as well as the smooth extrusion of ink through the needle without clogging. However, due to the highly viscous nature of CNFs, obtaining the uniform dispersion is challenging using the conventional mechanical agitation approach. To address this issue, a vacuum planetary high-speed mixer, which possesses the capacity of mixing high viscous materials, was applied to treat the hybrid. After treatment at a rotating rate of 1500 rpm for 30 min, the dark, homogeneous, viscoelastic gels are generated, which show tunable gel strength as a function of CNF loading (Figure S9, Supporting Information).

For the 3D printing technique based on direct ink writing, the printability of ink (e.g., extrudability, filament formation, shape fidelity, and geometrical accuracy) greatly depends on its rheological properties.[28] A 3D printable ink should possess 1) superior shear-thinning ability, enabling the smooth extrusion of ink through deposition nozzle under shear force and formation of smooth filament; 2) outstanding thixotropic property, allowing a rapid recovery in viscosity or viscoelasticity after 3D printing; and 3) an appropriate yield stress and storage modulus to achieve high shape fidelity of printed 3D constructs without deformation and collapsing (**Figure 3**a). Therefore, the rheological properties of the Mxene-based gel inks, including steady-state viscosity and shear stress (Figure 3b,c), thixotropic behavior (Figure 3d), and viscoelastic properties (Figure 3e), were comprehensively studied. As shown in Figure 3b, the viscosity of the gel inks is gradually increased with an increase in CNF loading, and the whole inks demonstrate a distinct shear thinning behavior due to the destruction of network structure under high shear stress. The shear-thinning behavior is essential for 3D printable ink because that could guarantee the ink to uniformly flow out a narrow orifice driven by the printing pressure.[14a,29] Interestingly, the MXene/CNF10 ink even presents higher viscosity values than these from highly concentrated pure MXene inks reported previously (e.g., 28.9 and 70 wt%) by one order of magnitude,[14b,30] indicating that high-aspect-ratio CNFs are effective to form a robust gel network with MXene nanosheets, leading to the formation of 3D printable ink at a much lower solid content of only 8 wt%. The curves of shear stress versus shear rate (Figure 3c) were well fitted by the power law (equation in Figure 3c and detailed in the Supporting information). The calculated values of the parameter n (i.e., flow behavior index) in Table S1 in the Supporting Information are <1, indicating that the inks are a typical non-Newtonian fluid

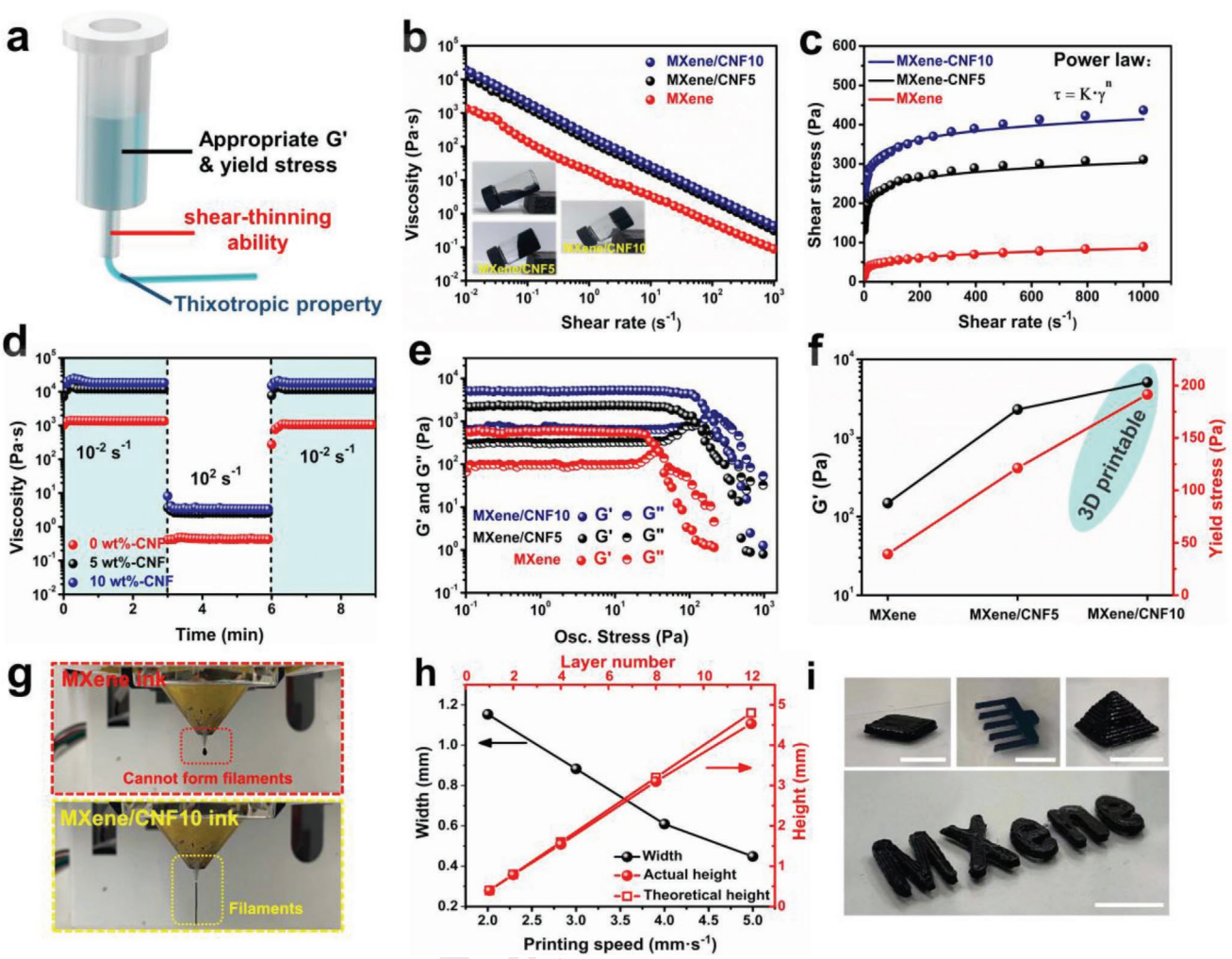

Figure 3. Rheology properties and 3D printability of the MXene/CNF gel inks: a) Schematic diagram of the rheological properties required for 3D printable gel inks. b) The viscosity as a function of shear rate; inset is the digital images of the pure MXene, MXene/CNF5, and MXene/CNF10 gel inks, all solid concentration of gel inks is 8 wt%. c) Shear stress as a function of shear rate, and the curves are fitted by the power law. d) Viscosity evolution over time for alternating low (10^{-2} s^{-1}) and high shear rates (10^{2} s^{-1}). e) G' and G'' as a function of oscillatory stress. f) G' at plateau regions and yield stress obtained at the crossover point between G' and G''. g) Digital appearance of MXene and MXene/CNF10 inks upon extruding. h) The width of the extruded MXene/CNF10 filaments on a glass substrate under different substrate moving speeds, as well as the actual height and theoretical height of the 3D printed MXene/CNF10 block architectures with different layers; note: the theoretical height is calculated based on the designed block models. i) Different 3D printed architectures using the MXene/CNF10 ink, including block (2 layers, scale bar: 5 mm), pectinate structure (2 layers, scale bar: 10 mm), pyramid (12 layers, scale bar: 10 mm), and MXene font (3 layers, scale bar: 10 mm).

with shear-thinning peculiarity.[4] Additionally, the K value (i.e., consistency coefficient) of MXene, MXene/CNF5, and MXene/CNF10 inks are 21.35, 161.13, and 234.78, respectively; which also reveals that the more CNFs in the ink, the higher the viscosity of the ink is.[31] The thixotropic behavior was investigated by monitoring the change in viscosity when the alternating low and high shear rates were applied (Figure 3d). Initially, to simulate the pre-extrusion condition, an extremely low shear rate of 10^{-2} s^{-1} was applied. After being continuously shear-mixed for 3 min, the shear rate was raised to 10^{2} s^{-1}, modeling the ink extrusion process through narrow nozzle. It was observed that the viscosity promptly dropped while the higher shear rate was applied. At this stage, the MXene/CNF gel network destroyed and its structural units responded to the shear stress by aligning themselves in the direction of flow, hence exhibiting strong shear-thinning behavior that enables the ink to flow out the nozzle (Figure 3b). Finally, when the shear rate was returned to 10^{-2} s^{-1}, the viscosity instantaneously recovered as a result of the restoration of MXene/CNF gel network. The inks show different viscosity recovery percentages depending on the CNF loading and recovery time. At a recovery time of 3 min, the viscosity recovery percentages of MXene, MXene/CNF5, and MXene/CNF10 inks are 87.74%, 98.51%, and 99.12%, respectively. These observations demonstrate that the MXene/CNF10 ink could fleetly restored its original state and maintain stable as-printed architecture after extrusion during the 3D printing process. The viscoelastic properties of MXene/CNF inks were further examined by dynamic rheological measurements as functions of oscillatory stress and angular frequency. Obviously, the whole inks present predominantly solid-like behavior at the

region below the crossover point ($G' > G''$). When the stress increases above the yield stress (i.e., the stress at the crossover point of $G' = G''$), however, the networked structure breaks and thus the solid to liquid transition occurs (Figure 3e). The magnitude of the G' at the plateau region (i.e., the region where G' is almost independent of stress) and yield stress increase as the CNF loading becomes higher (Figure 3f). Especially for the MXene/CNF10 ink, the G' at the plateau region and yield stress reach the highest values of ≈5100 and 191.56 Pa, respectively. Furthermore, the angular frequency sweeping measurements also reveal that the MXene/CNF10 inks maintained high G' and complex modulus independent of angular frequency (Figure S10, Supporting Information). The high modulus and yield stress of the MXene/CNF10 ink represent a stiffer peculiarity which is desirable for the self-standing architecture without deformation. Figure S11 in the Supporting Information displays the TEM image of the diluted MXene/CNF10 ink, in which the MXene nanosheet is wrapped by the entangled CNFs network. This unique structure of 2D material wrapped by 1D entanglement network is responsible for improving rheological properties. Taken together, the exceptional rheological properties of the MXene/CNF10 ink, including significant shear-thinning capacity, superior thixotropic behavior, and high G' as well as yield stress, ensure their good 3D printability, which will be discussed in the following section.

The as-prepared gel inks were loaded into the syringe attached with a needle having a diameter of 0.4 mm to examine the 3D printability. A Dr. INVIVO 4D bioprinter (ROKIT Healthcare, INC, South Korea) equipped with a pneumatic dispenser was applied for 3D printing. Upon extrusion, the pure MXene ink with low viscosity generated droplets (Figure 3g, top), leading to discontinuous flow, i.e., poor extrudability. By contrast, the uniform, continuous filament was extruded using the MXene/CNF10 ink (Figure 3g, bottom) ascribing to its homogeneity and improved rheological performance. Then, through simply extruding a linear filament on a glass substrate, we evaluated the filament formation as a function of substrate moving speed (i.e., printing speed) (Figure S12, Supporting Information). It was found that the minimum pressure required for extrusion is 35 kPa. At this condition, the width of filament gradually decreases from 1.15 to 0.44 mm as the substrate moving speed increases from 2 to 5 mm s^{-1} (Figure 3h). Further increase in the substrate moving speed leads to breakage of filament, which is undesirable. The minimum width of 0.44 mm is slightly wider than the diameter of the nozzle (i.e., 0.40 mm), which is probably due to the post-extruding swelling behavior as reported in previous study.[32] The shape fidelity was further examined through 3D printing of block architectures with different layers (Figure S13, Supporting Information). The actual and theoretical heights of the 3D printed block as a function of layer number was directly contrasted. As shown in Figure 3h, the one single layer has a height of 0.39 mm, and the blocks with 2, 4, 8, and 12 layers have heights of 0.79, 1.54, 3.10, and 4.54 mm, respectively. The actual heights are close to the theoretical heights, despite the slight discrepancy appears as more layers are deposited. Due to the excellent 3D printability of MXene/CNF10 ink, a variety of 3D architectures, including block, pectinate structure, pyramid, and MXene font, were successfully printed, all of which exhibit highly geometrical accuracy without deformation and collapse (Figure 3i).

Previous investigations reported that direct drying of the 3D printed MXene-based architecture led to shrinkage along the width, length and height of architecture due to the presence of a large amount of water in the ink.[14b] Herein, freeze-drying strategy was employed to maintain the internal integrity and the external shape of 3D printed MXene/CNF10 architectures. This resulted in minimal shrinkage, despite our 3D printed MXene/CNF10 architectures contain a much larger portion of water (i.e., ≈92 wt%). **Figure 4**a,d shows the top and side view SEM images of freeze-dried, 3D printed MXene/CNF10 block architecture with two deposition layers, respectively. From the top-view SEM image, the tightly connected filaments of ≈0.43 mm in diameter appears, exhibiting minimal shrinkage compared with the filament in a gel state (i.e., 0.44 mm in diameter). The edge-view SEM image shows the clear boundary between two individual filament layers with a total height of ≈0.78 mm, which is close to the height of 3D printed gel block (i.e., 0.79 mm) as well. The exceptional viscoelastic properties and freeze-drying technique are responsible for the stable configuration without severe internal collapse. Furthermore, the highly porous structure appeared both on the surface and inside of freeze-dried block architecture (Figure 4b,c,e,f). The cross-sectional image (Figure 4f) displays an internal network with interconnected pores ranging from 4 to 24 μm in diameter, caused by the sublimation of ice crystals during freeze-drying. Besides, Ti, C, O, and F elements are uniformly distributed in the cross-section (Figure 4g), suggesting the homogeneous mixing of CNFs and MXene. Based on the N_2 adsorption and desorption isotherms (Figure 4h), the 3D printed block architecture shows a specific surface area of 78.13 m^2 g^{-1}, which is predominantly contributed by the mesoporous internal structures indicated by the typical IV adsorption/desorption isotherm. The specific surface area of the 3D printed MXene/CNF block architecture is much higher than those of MXene-based films/aerogels (i.e., 30.9 and 16.2 m^2 g^{-1}) prepared by conventional fabrication techniques.[33] In fact, the conventional fabrication techniques (e.g., vacuum filtration or casting) always give rise to the restacking of MXene nanosheets, leading to the low surface utilization of the MXene-based electrode.[10,34] By constant, the integration of 3D printing technique and post freeze-drying treatment in this work leads to assembly of the 2D MXene nanosheets and 1D CNFs into a porous structure within the architecture. Meanwhile, CNFs might act as intercalating agents, which prevents normal restacking of MXene nanosheets (Figure S14, Supporting Information), and therefore improve their surface area accessibility.

To confirm the interaction between CNFs and MXene, the microstructure of 3D printed MXene/CNF block architecture was further investigated using X-ray diffraction (XRD), X-ray photoelectron spectroscopy (XPS), and FTIR analyses. As shown in Figure 4i, after the inclusion of CNFs, the characteristic (002) peak of MXene shifts from 6.02°to 5.88°, proving the successful intercalation of CNFs into MXene nanosheets.[1d] Then, the question is raised why CNFs are capable of intercalating and what the driving force is for their intercalation. To this end, XPS and FTIR spectra were recorded (Figures S15 and S16, Supporting Information). From the high-resolution C 1s

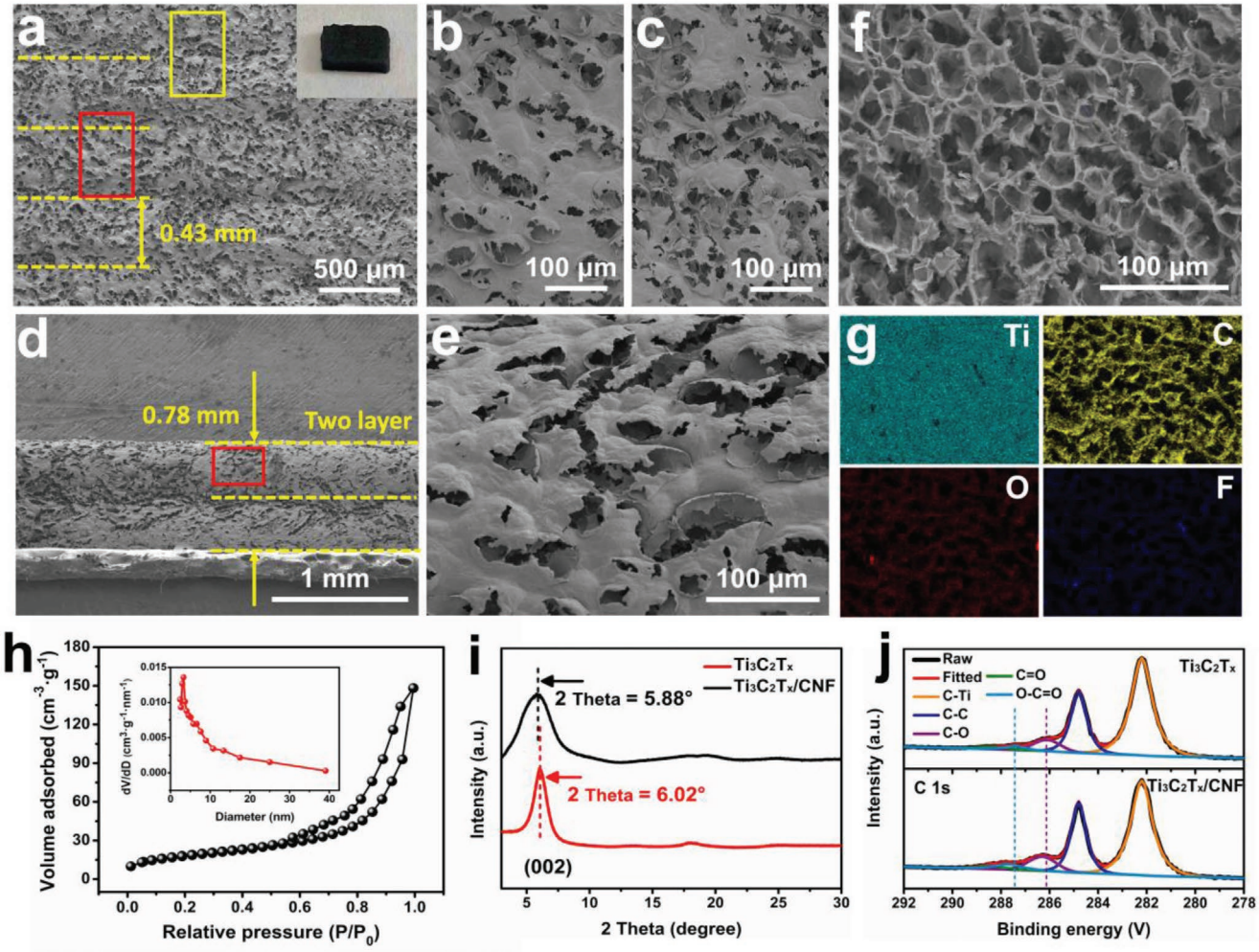

Figure 4. Morphology and chemical structure of 3D printed, freeze-dried MXene/CNF10 block: a) Top view SEM image; inset is the digital appearance. b,c) The enlarged SEM images corresponding to the red and yellow frame parts in panel (a), respectively. d) Side view SEM image. e) The enlarged SEM image corresponding to the red frame part in panel (d). f) Cross-sectional SEM image. g) The corresponding EDS mapping of Ti, C, O, and F elements. h) N_2 adsorption and desorption isotherms; the inset is pore size distribution, which displays a main pore size centered at the 3.26 nm. i) XRD patterns. j) High-resolution C 1s spectra.

spectra (Figure 4j), as the CNFs are compounded, the binding energy peaks of C—O and C=O groups increases from 286.1 and 287.4 eV to 286.3 and 287.8 eV, respectively. More importantly, the absorption peak of —OH group at 3421 cm^{-1} in FTIR spectra also shifts to 3416 cm^{-1} in the presence of CNFs (Figure S16, Supporting Information). These results reveal that the formation of strong hydrogen bonding between MXene and CNFs is the main driving force for intercalation, which agree well with the previous studies.[35] Consequently, the 3D printed porous MXene/CNF architectures exhibit favorable mechanical performance, as demonstrated by tensile and compression tests (Figure S17, Supporting Information). The 3D printed rectangle block with three layers has the tensile strength and modulus up to 0.225 and 5.733 MPa, respectively. The 3D printed quadrate block with six layers has the compressive modulus of 0.338 MPa, and the compressive strength of 0.258 MPa at strain of 80%.

The hierarchically porous structure of 3D printed block as well as the inherent electrochemical activity of MXene allow us to explore its potential in the energy storage application as a freestanding electrode. The electrochemical measurements for the 3D printed MXene/CNF10 block were carried out using a typical three-electrode system in 1 M H_2SO_4 and the corresponding results are shown in **Figure 5**. The Cyclic voltammetry (CV) profiles (Figure 5a) display a pair of signature redox peaks associated with the protonation and change in the oxidation states of Ti atoms, suggesting the typical pseudocapacitive behavior of MXene.[1d] Figure 5b shows the galvanostatic charge–discharge (GCD) profiles at various current densities from 1 to 20 mA cm^{-2}. All the curves show a nearly symmetrical nonlinear triangle, indicating the good reversibility in the charging/discharging process as well as the pseudocapacitive nature of MXene. The rate performance obtained from the GCD curves exhibits a favorable areal capacitance value of 2.43 F cm^{-2} (84.6 F g^{-1}) at 1 mA cm^{-2} associated with high retention of ≈70% at 20 mA cm^{-2} (1.72 F cm^{-2}/59.6 F g^{-1}). This suggests the good rate performance and high surface utilization of MXene in 3D printed electrode (Figure 5c). The remarkable

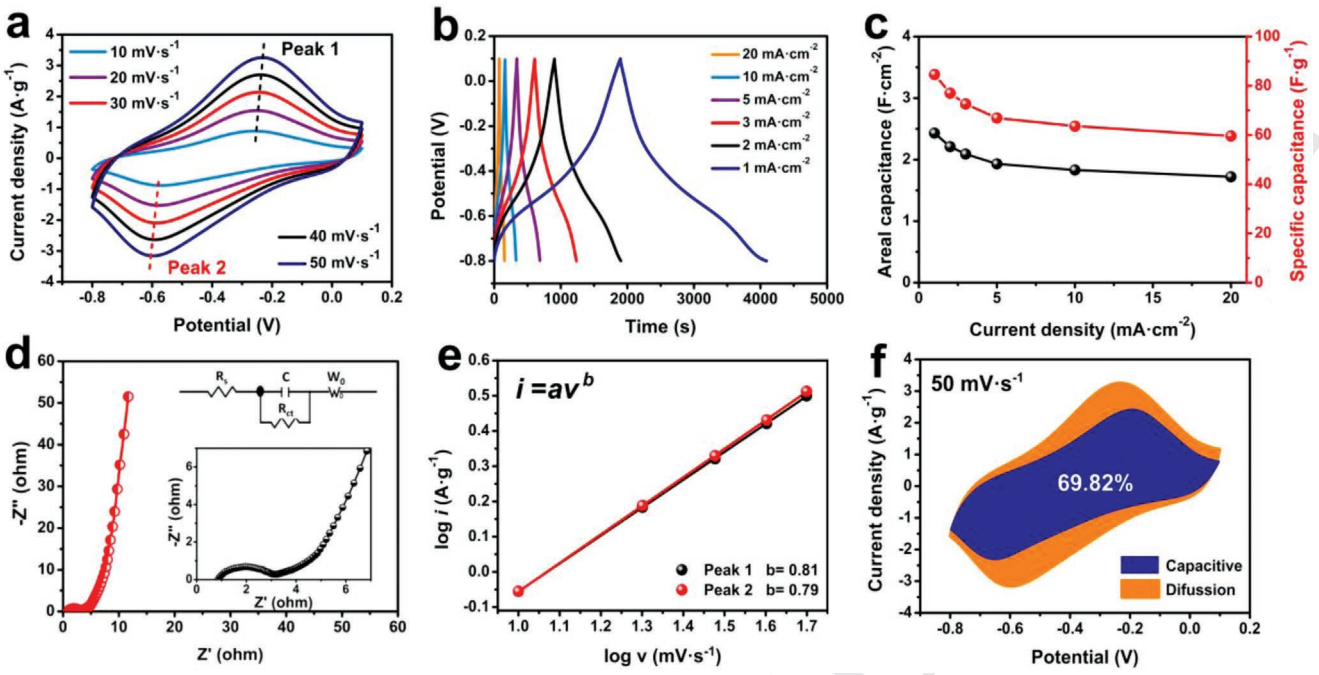

Figure 5. Electrochemical performance of the 3D printed, freeze-dried MXene/CNF10 block in 1 M H_2SO_4 electrolyte: a) CV profiles at different scan rates (10–50 mV s^{-1}). b) GCD profile at various current densities (1–20 mA cm^{-2}). c) The areal and specific capacitance at various current densities. d) Nyquist plots. e) Logarithm plot of peak currents as function of scan rates. f) CV profile at 50 mV s^{-1} with the blue area representing the surface capacitive contribution.

electrochemical performance of 3D printed block electrode can be ascribed to 1) high conductivity of MXene, ensuring efficient current collection; and 2) the 3D hierarchically pore structure, facilitating efficient infiltration of the electrolyte and allowing the fast diffusion of ions, as proved by the Nyquist plots in Figure 5d. The nearly vertical line in the low-frequency region suggests the facile ion diffusion owing to the presence of a highly porous structure, while the small semicircle in the medium-frequency region reveals that the addition of only 10 wt% CNFs did not cause a large charge-transfer resistance.[36] To quantitatively determine the equivalent series resistance (R_s) and the charge transfer resistance (R_{ct}), an electric equivalent circuit was used, as shown in the inset of Figure 5d. The R_s and R_{ct} values were determined to be 0.87 and 2.87 Ω, respectively; indicating the good conductivity and electron transfer capacity of the block electrode.

The charge storage kinetics analysis was carried out from the CV curves using the following equation[36]

$$i = av^b \tag{1}$$

where a and b values are determined from the slope of the peak current (i) versus scan rate (v), and the b value of 0.5 and 0.1 represent the diffusion control behavior and surface capacitive behavior, respectively. Interestingly, the b-value corresponding to the two peak currents is calculated as 0.81 and 0.79, respectively (Figure 5e). These values are between 0.5 and 1, indicating that the charge storage process of the block involves both the diffusion control and surface capacitive. To quantify the capacitive and diffusion-control contributions to the total capacitance, a closer examination of the CV curves was performed according to the following relationship[2b]

$$\log(i) = b\log(v) + \log(a) \tag{2}$$

where i(V) is the current at a given potential in CV profile, and k_1v and $k_2v^{(1/2)}$ are corresponding to the surface capacitive contribution and diffusion-control contribution, respectively. As shown in Figure 5f and Figure S18 in the Supporting Information, the surface capacitive contribution increases from 51.03% at 10 mV s^{-1} to 69.82% at 50 mV s^{-1}. The high capacitive behavior for the charge storage further demonstrate the excellent electrochemical performance of the porous MXene–CNF block.[10]

To provide a proof-of-concept design, a solid-state interdigitated SSC device was assembled using two 3D printed, freeze-dried MXene/CNF10 pectinate architecture as electrodes and the PVA/H_2SO_4 gel as electrolyte (**Figure 6**a). The detailed information on the dimension of 3D printed pectinate architecture is provided in Figure S19 in the Supporting Information. The CV curves of the SSC at various scan rates present a similar shape (Figure 6b), revealing an ideal capacitive behavior. The GCD curves at the different current densities exhibit a triangular and symmetric shape (Figure 6c), also suggesting typical capacitive characteristics and superior charge storage ability.[1d,10,37] Our SSC device achieves areal capacitances of 2.02 F cm^{-2} (specific capacitance of 69.9 F g^{-1}) at 1 mA cm^{-2} and 1.14 F cm^{-2} (specific capacitance of 39.4 F g^{-1}) at 20 mA cm^{-2} (Figure 6d), surpassing the capacitance performance of most of previously reported MXene-based hybrids (Tables S3 and S4, Supporting information), such as MXene/CNF/PC (143 mF cm^{-2}),[36] $Ti_3C_2T_x$/silver-plated nylon fiber (328 mF cm^{-2}),[38] $Ti_3C_2T_x$/graphene fibers (372 mF cm^{-2}).[39] Furthermore, the volumetric capacitance of the SSC device reaches 25.4 F cm^{-3} at 1 mA cm^{-2} and retains

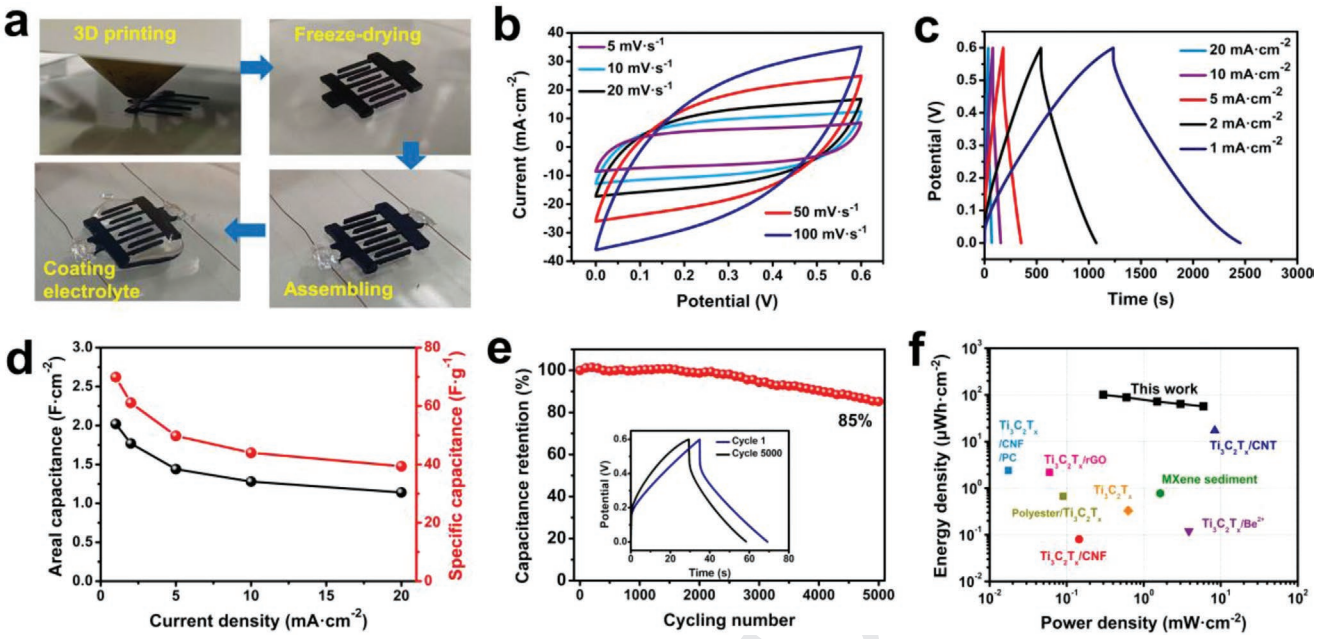

Figure 6. Electrochemical performance of the symmetric supercapacitor device: a) Digital images of the fabrication process. b) CV profiles at various scan rates ranging from 5 to 100 mV s^{-1}. c) GCD profile at various current densities ranging from 1 to 20 mA cm^{-2}. d) The areal and specific capacitance. e) Cycling performance of the SSC device measured at 20 mA cm^{-2}; inset is the GCD profile at first cycle and after 5000 cycles. f) Ragone plots of our device in comparison with other reported devices in terms of energy and powder densities.

14.3 F cm^{-3} at 20 mA cm^{-2} (Figure S20, Supporting Information). Long-term cycling stabilities of the device at high current density (20 mA cm^{-2}) are exhibited in Figure 6e. Remarkably, the capacitance of 1.72 F cm^{-2} (≈85% of the initial value) was maintained after 5000 cycles. Figure S21 in the Supporting Information presents the CV profile and Nyquist plot before and after cycling measurement. The area of the CV profile decreases but the profile maintains a rectangular-like shape (Figure S21a, Supporting Information). Besides, the charge transfer resistance (R_{ct}) associated with the semicircle diameter in high frequency region slightly increases from 3.06 to 3.49 Ω (Figure S21b, Supporting Information). These results indicate that the SSC retains the favorable charge transfer ability and capacitive behavior after cycling. It should be noted that the current leakage is an non-negligible issue for supercapacitor. We therefore conducted the self-discharge measurement to evaluate the potential influence of leakage current. The device was charged to 0.6 V at a current density of 1 mA cm^{-2} and then the change of potential with time under open circuit condition was monitored. As shown in Figure S22 in the Supporting Information, the potential shows a retention of 78.36% after 5 h. The decay rate of the potential is calculated as ≈7.2 μV s^{-1}, which is close to the small value reported in previous study,[40] indicating that the leakage current would not seriously affect the electrochemical performance. Figure 6f enumerates the Ragone plots of the device in this work together with other reported devices in terms of energy and power densities.[1d,36,41] The solid-state SSC device demonstrates an energy density of 101 μWh cm^{-2} at a power density of 0.299 mW cm^{-2} and retains 57 μWh cm^{-2} at the power density of 5.983 mW cm^{-2}, which are orders of magnitude higher than that of ever-reported MXene-based devices (Table S3, Supporting Information). Finally, a tandem device was fabricated by connecting four devices in series to deliver a voltage of 2.4 V. This tandem device can directly power a digital watch (Figure S23, Supporting Information) after charging, exemplifying the viability of our 3D printed SSC device toward practical application.

3. Conclusion

In summary, we successfully enhanced the 3D printability of MXene-based inks at low MXene loadings using CNFs as rheological modifiers through rationally controlling the dimension and surface chemistry of CNFs during TEMPO-mediated oxidation process. In addition to rheological modification, CNFs acted as intercalating agents as well, which prevents normal restacking of MXene nanosheets, leading to the formation of highly freestanding, hierarchically porous architectures after freeze-drying. Such well-designed porous structure associated with high electrical conductivity of MXene allow fast electron conduction and ion diffusion, giving rise to favorable capacitance and rate performance. As a proof of concept, a solid-state interdigitated SSC device was successfully fabricated through 3D printing. The SSC device demonstrates a high areal capacity (2.02 F cm^{-2}, at 1 mA cm^{-2}), an outstanding rate capability (1.14 F cm^{-2}, at 20 mA cm^{-2}), and an excellent cycling stability with retention of 85% over 5000 cycles. More importantly, the SSC device delivers an energy density of 101 μWh cm^{-2} at the power density of 0.299 mW cm^{-2}, and the volumetric capacitance of 25.4 F cm^{-3} at 1 mA cm^{-2}. We anticipate that the energy and power densities can be further improved through rational design of electrode architecture by 3D printing, introduction of other active materials as well as optimization on the

electrolytes. It is also expected that our developed MXene/CNF inks with outstanding rheological properties and 3D printability can be extended to fabricate other energy storage and conversion devices that require well-customized architecture design.

Supporting Information

Supporting Information is available from the Wiley Online Library or from the author.

Acknowledgements

This work was supported from the Natural Science Foundation of Jiangsu Province (BK20200776), the Jiangsu Agriculture Science and Technology Innovation Fund (CX(20)3054), and the Jiangsu Specially-Appointed Professor Program. The authors also thank the Advanced Analysis Testing Center, Nanjing Forestry University, for SEM, XPS, XRD, and rheology characterization.

Conflict of Interest

The authors declare no conflict of interest.

Author Contributions

All authors contributed equally to this work and gave approval to the final version of the manuscript.

Data Availability Statement

The data that support the findings of this study are available from the corresponding author upon reasonable request.

Keywords

3D printing, cellulose nanofibers, energy storage, MXene, rheological properties

Received: September 22, 2021
Revised: November 12, 2021
Published online:

[1] a) N. A. Kyeremateng, T. Brousse, D. Pech, *Nat. Nanotechnol.* **2017**, *12*, 7; b) X. L. Dong, Z. Y. Guo, Y. F. Song, M. Y. Hou, J. Q. Wang, Y. G. Wang, Y. Y. Xia, *Adv. Funct. Mater.* **2014**, *24*, 3405; c) Y. Y. Peng, B. Akuzum, N. Kurra, M. Q. Zhao, M. Alhabe, B. Anasori, E. C. Kumbur, H. N. Alshareef, M. D. Ger, Y. Gogotsi, *Energy Environ. Sci.* **2016**, *9*, 2847; d) W. Q. Tian, A. VahidMohammadi, M. S. Reid, Z. Wang, L. Q. Ouyang, J. Erlandsson, T. Pettersson, L. Wagberg, M. Beidaghi, M. M. Hamedi, *Adv. Mater.* **2019**, *31*, 1902977.

[2] a) Z. D. Fan, J. Jin, C. Li, J. S. Cai, C. H. Wei, Y. L. Shao, G. F. Zou, J. Y. Sun, *ACS Nano* **2021**, *15*, 3098; b) K. Li, X. H. Wang, S. Li, P. Urbankowski, J. M. Li, Y. X. Xu, Y. Gogotsi, *Small* **2020**, *16*, 1906581; c) T. Yun, G. S. Lee, J. Choi, H. Kim, G. G. Yang, H. J. Lee, J. G. Kim, H. M. Lee, C. M. Koo, J. Lim, S. O. Kim, *ACS Nano* **2021**, *15*, 10058.

[3] a) K. Shen, B. Li, S. B. Yang, *Energy Storage Mater.* **2020**, *24*, 670; b) Y. K. Pang, Y. T. Cao, Y. H. Chu, M. H. Liu, K. Snyder, D. MacKenzie, C. Y. Cao, *Adv. Funct. Mater.* **2020**, *30*, 1906244; c) Z. Y. Lyu, G. J. H. Lim, R. Guo, Z. H. Pan, X. Zhang, H. Zhang, Z. M. He, S. Adams, W. Chen, J. Ding, J. Wang, *Energy Storage Mater.* **2020**, *24*, 336; d) T. T. Gao, Z. Zhou, J. Y. Yu, J. Zhao, G. L. Wang, D. X. Cao, B. Ding, Y. J. Li, *Adv. Energy Mater.* **2019**, *9*, 1802578; e) V. Egorov, U. Gulzar, Y. Zhang, S. Breen, C. O'Dwyer, *Adv. Mater.* **2020**, *32*, 2000556.

[4] M. C. Li, Q. L. Wu, R. J. Moon, M. A. Hubbe, M. J. Bortner, *Adv. Mater.* **2021**, *33*, 2006052.

[5] a) X. W. Tang, Z. Han, T. X. Fan, *Abstr. Pap. Am. Chem. Soc.* **2018**, *256*, 3502; b) B. Yao, S. Chandrasekaran, J. Zhang, W. Xiao, F. Qian, C. Zhu, E. B. Duoss, C. M. Spadaccini, M. A. Worsley, Y. Li, *Joule* **2019**, *3*, 459.

[6] B. L. Chen, Y. Z. Jiang, X. H. Tang, Y. Y. Pan, S. Hu, *ACS Appl. Mater. Interfaces* **2017**, *9*, 28433.

[7] X. Aeby, A. Poulin, G. Siqueira, M. K. Hausmann, G. Nystrom, *Adv. Mater.* **2021**, *33*, 2101328.

[8] a) M. Alhabeb, K. Maleski, B. Anasori, P. Lelyukh, L. Clark, S. Sin, Y. Gogotsi, *Chem. Mater.* **2017**, *29*, 7633; b) M. Naguib, M. Kurtoglu, V. Presser, J. Lu, J. J. Niu, M. Heon, L. Hultman, Y. Gogotsi, M. W. Barsoum, *Adv. Mater.* **2011**, *23*, 4248.

[9] W. T. Cao, F. F. Chen, Y. J. Zhu, Y. G. Zhang, Y. Y. Jiang, M. G. Ma, F. Chen, *ACS Nano* **2018**, *12*, 4583.

[10] K. Li, M. Y. Liang, H. Wang, X. H. Wang, Y. S. Huang, J. Coelho, S. Pinilla, Y. L. Zhang, F. W. Qi, V. Nicolosi, Y. X. Xu, *Adv. Funct. Mater.* **2020**, *30*, 2000842.

[11] G. B. Ying, A. D. Dillon, A. T. Fafarman, M. W. Barsoum, *Mater. Res. Lett.* **2017**, *5*, 391.

[12] a) C. F. Zhang, L. McKeon, M. P. Kremer, S. H. Park, O. Ronan, A. Seral-Ascaso, S. Barwich, C. O. Coileain, N. McEvoy, H. C. Nerl, B. Anasori, J. N. Coleman, Y. Gogotsi, V. Nicolosi, *Nat. Commun.* **2019**, *10*, 1795; b) S. Uzun, M. Schelling, K. Hantanasirisakul, T. S. Mathis, R. Askeland, G. Dion, Y. Gogotsi, *Small* **2021**, *17*, 2006376.

[13] a) S. K. Xu, Y. Dall'Agnese, G. D. Wei, C. Zhang, Y. Gogotsi, W. Han, *Nano Energy* **2018**, *50*, 479; b) H. B. Hu, T. Hua, *J. Mater. Chem. A* **2017**, *5*, 19639.

[14] a) W. J. Yang, J. Yang, J. J. Byun, F. P. Moissinac, J. Q. Xu, S. J. Haigh, M. Domingos, M. A. Bissett, R. A. W. Dryfe, S. Barg, *Adv. Mater.* **2019**, *31*, 1902725; b) J. Orangi, F. Hamade, V. A. Davis, M. Beidaghi, *ACS Nano* **2020**, *14*, 640.

[15] a) S. Jambhulkar, S. Y. Liu, P. Vala, W. H. Xu, D. Ravichandran, Y. X. Zhu, K. Bi, Q. Nian, X. F. Chen, K. N. Song, *ACS Nano* **2021**, *15*, 12057; b) Y. B. Zhang, G. Shi, J. D. Qin, S. E. Lowe, S. Q. Zhang, H. J. Zhao, Y. L. Zhong, *ACS Appl. Electron. Mater.* **2019**, *1*, 1718.

[16] Y. Z. Zhang, Y. Wang, Q. Jiang, J. K. El-Demellawi, H. Kim, H. N. Alshareef, *Adv. Mater.* **2020**, *32*, 1908486.

[17] a) R. Ajdary, S. Q. Huan, N. Z. Ezazi, W. C. Xiang, R. Grande, H. A. Santos, O. J. Rojas, *Biomacromolecules* **2019**, *20*, 2770; b) L. Wei, S. Chuanling, D. Haishun, Z. Miaomiao, Z. Xinyu, X. Hongxiang, *J. For. Eng.* **2019**, *4*, 11.

[18] a) M. K. Hausmann, G. Siqueira, R. Libanori, D. Kokkinis, A. Neels, T. Zimmermann, A. R. Studart, *Adv. Funct. Mater.* **2020**, *30*, 1904127; b) Y. Chen, Z. Y. Yu, Y. H. Ye, Y. F. Zhang, G. Y. Li, F. Jiang, *ACS Nano* **2021**, *15*, 1869; c) K. M. O. Hakansson, I. C. Henriksson, C. D. Vazquez, V. Kuzmenko, K. Markstedt, P. Enoksson, P. Gatenholm, *Adv. Mater. Technol.* **2016**, *1*, 1600096.

[19] a) S. Sultan, H. N. Abdelhamid, X. D. Zou, A. P. Mathew, *Adv. Funct. Mater.* **2019**, *29*, 1805372; b) D. X. Cao, Y. J. Xing, K. Tantratian, X. Wang, Y. Ma, A. Mukhopadhyay, Z. Cheng, Q. Zhang, Y. C. Jiao, L. Chen, H. L. Zhu, *Adv. Mater.* **2019**, *31*, 1807313; c) Y. Y. Li, H. L. Zhu, Y. B. Wang, U. Ray, S. Z. Zhu, J. Q. Dai, C. J. Chen, K. Fu,

S. H. Jang, D. Henderson, T. Li, L. B. Hu, *Small Methods* **2017**, *1*, 1700222.
[20] S. Shinoj, R. Visvanathan, S. Panigrahi, M. Kochubabu, *Ind. Crops Prod.* **2011**, *33*, 7.
[21] J. Lamaming, R. Hashim, O. Sulaiman, C. P. Leh, T. Sugimoto, N. A. Nordin, *Carbohydr. Polym.* **2015**, *127*, 202.
[22] a) A. Isogai, *Adv. Mater.* **2021**, *33*, 2000630; b) W. Bo, L. Mengting, S. Faning, C. Mengwei, X. Lingxiang, X. Zhaohui, H. Wen, *J. For. Eng.* **2019**, *4*, 94.
[23] W. S. Chen, H. P. Yu, S. Y. Lee, T. Wei, J. Li, Z. J. Fan, *Chem. Soc. Rev.* **2018**, *47*, 2837.
[24] S. Shin, J. Hyun, *Carbohydr. Polym.* **2021**, *263*, 117976.
[25] a) S. R. D. Petroudy, J. Ranjbar, E. R. Garmaroody, *Carbohydr. Polym.* **2018**, *197*, 565; b) T. Saito, Y. Nishiyama, J. L. Putaux, M. Vignon, A. Isogai, *Biomacromolecules* **2006**, *7*, 1687.
[26] a) J. Q. Zhang, L. J. Wan, Y. Gao, X. L. Fang, T. Lu, L. K. Pan, F. Z. Xuan, *Adv. Electron. Mater.* **2019**, *5*, 1900285; b) A. Lipatov, M. Alhabeb, M. R. Lukatskaya, A. Boson, Y. Gogotsi, A. Sinitskii, *Adv. Electron. Mater.* **2016**, *2*, 1600255.
[27] Z. Fan, C. Wei, L. Yu, Z. Xia, J. Cai, Z. Tian, G. Zou, S. X. Dou, J. Sun, *ACS Nano* **2020**, *14*, 867.
[28] S. C. Lee, G. Gillispie, P. Prim, S. J. Lee, *Chem. Rev.* **2020**, *120*, 10797.
[29] a) G. Siqueira, D. Kokkinis, R. Libanori, M. K. Hausmann, A. S. Gladman, A. Neels, P. Tingaut, T. Zimmermann, J. A. Lewis, A. R. Studart, *Adv. Funct. Mater.* **2017**, *27*, 1604619; b) M. Cheng, R. Deivanayagam, R. Shahbazian-Yassar, *Batteries Supercaps* **2020**, *3*, 130.
[30] B. Akuzum, K. Maleski, B. Anasori, P. Lelyukh, N. J. Alvarez, E. C. Kumbur, Y. Gogotsi, *ACS Nano* **2018**, *12*, 2685.
[31] C. Z. Liu, M. C. Li, C. T. Mei, W. M. Chen, J. Q. Han, Y. Y. Yue, S. X. Ren, A. D. French, G. M. Aita, G. Eggleston, Q. L. Wu, *Ind. Crops Prod.* **2020**, *150*, 112378.
[32] A. I. Cernencu, A. Lungu, I. C. Stancu, A. Serafim, E. Heggset, K. Syverud, H. Iovu, *Carbohydr. Polym.* **2019**, *220*, 12.
[33] a) S. Xu, G. Wei, J. Li, Y. Ji, N. Klyui, V. Izotov, W. Han, *Chem. Eng. J.* **2017**, *317*, 1026; b) X. Wang, Q. Fu, J. Wen, X. Ma, C. Zhu, X. Zhang, D. Qi, *Nanoscale* **2018**, *10*, 20828.
[34] Z. M. Fan, Y. S. Wang, Z. M. Xie, D. L. Wang, Y. Yuan, H. J. Kang, B. L. Su, Z. J. Cheng, Y. Y. Liu, *Adv. Sci.* **2018**, *5*, 1800750.
[35] a) S. J. Wan, X. Li, Y. L. Wang, Y. Chen, X. Xie, R. Yang, A. P. Tomsia, L. Jiang, Q. F. Cheng, *Proc. Natl. Acad. Sci. USA* **2020**, *117*, 27154; b) B. Zhou, Z. Zhang, Y. L. Li, G. J. Han, Y. Z. Feng, B. Wang, D. B. Zhang, J. M. Ma, C. T. Liu, *ACS Appl. Mater. Interfaces* **2020**, *12*, 4895.
[36] W. M. Chen, D. T. Zhang, K. Yang, M. Luo, P. Yang, X. Y. Zhou, *Chem. Eng. J.* **2021**, *413*, 127524.
[37] F. Wang, X. L. Liu, G. G. Duan, H. Q. Yang, J. Y. Cheong, J. Lee, J. Ahn, Q. Zhang, S. J. He, J. Q. Han, Y. Zhao, I. D. Kim, S. H. Jiang, *Small* **2021**, *17*, 2102532.
[38] M. M. Hu, Z. J. Li, G. X. Li, T. Hu, C. Zhang, X. H. Wang, *Adv. Mater. Technol.* **2017**, *2*, 1700143.
[39] Q. Y. Yang, Z. Xu, B. Fang, T. Q. Huang, S. Y. Cai, H. Chen, Y. J. Liu, K. Gopalsamy, W. W. Gao, C. Gao, *J. Mater. Chem. A* **2017**, *5*, 22113.
[40] a) J. Lin, C. G. Zhang, Z. Yan, Y. Zhu, Z. W. Peng, R. H. Hauge, D. Natelson, J. M. Tour, *Nano Lett.* **2013**, *13*, 72; b) J. Lin, Z. W. Peng, Y. Y. Liu, F. Ruiz-Zepeda, R. Q. Ye, E. L. G. Samuel, M. J. Yacaman, B. I. Yakobson, J. M. Tour, *Nat. Commun.* **2014**, *5*, 5714.
[41] a) J. X. Zhao, Y. Zhang, Y. A. Huang, X. X. Zhao, Y. H. Shi, J. Y. Qu, C. F. Yang, J. X. Xie, J. J. Wang, L. Li, Q. H. Yan, S. H. Hou, C. H. Lu, X. H. Xu, Y. G. Yao, *J. Mater. Chem. A* **2019**, *7*, 972; b) S. Abdolhosseinzadeh, R. Schneider, A. Verma, J. Heier, F. Nuesch, C. F. Zhang, *Adv. Mater.* **2020**, *32*, 2000716; c) S. Li, Q. Shi, Y. Li, J. Yang, T. H. Chang, J. W. Jiang, P. Y. Chen, *Adv. Funct. Mater.* **2020**, *30*, 2003721; d) C. F. Zhang, M. P. Kremer, A. Seral-Ascaso, S. H. Park, N. McEvoy, B. Anasori, Y. Gogotsi, V. Nicolosi, *Adv. Funct. Mater.* **2018**, *28*, 1705506; e) Y. Yue, N. Liu, Y. A. Ma, S. L. Wang, W. J. Liu, C. Luo, H. Zhang, F. Cheng, J. Y. Rao, X. K. Hu, J. Su, Y. H. Gao, *ACS Nano* **2018**, *12*, 4224.

ADVANCED FUNCTIONAL MATERIALS

Reprint Order Form

Please complete this form and return it via E-Mail to the Editorial Office:

Email: afm@wiley-vch.de

Manuscript No.:
Customer No.: (if available) _____
Purchase Order No.: _____
Author: _____

Charges for Reprints in Euro (excl. VAT), prices are subject to change. Minimum order 50 copies.

No. of pages	50 copies	100 copies	150 copies	200 copies	300 copies	500 copies
1– 4	345,—	395,—	425,—	445,—	548,—	752,—
5– 8	490,—	573,—	608,—	636,—	784,—	1077,—
9–12	640,—	739,—	786,—	824,—	1016,—	1396,—
13–16	780,—	900,—	958,—	1004,—	1237,—	1701,—
17–20	930,—	1070,—	1138,—	1196,—	1489,—	2022,—
every additional 4 pages	147,—	169,—	175,—	188,—	231,—	315,—

Information regarding VAT: The charges for publication of *cover pictures /reprints/issues/poster/Video abstracts/* are considered to be "supply of services" and therefore subject to German VAT. However, if you are an institutional customer outside Germany, the tax can be waived if you provide us with the valid VAT number of your company. Non-EU customers may have a VAT number starting with "EU" instead of their country code, if they are registered with the EU tax authorities. If you do not have a valid EU VAT number and you are a taxable person doing business in a non-EU country, please provide a certification from your local tax authorities confirming that you are a taxable person under local tax law. Please note that the certification must confirm that you are a taxable person and are conducting an economic activity in your country. **Note:** certifications confirming that you are a tax-exempt legal body (non-profit organization, public body, school, political party, etc.) in your country do not exempt you from paying German VAT.

Please send me send bill me for

☐ no. of reprints (minimum of 50 reprints)

☐ high-resolution PDF file (330 Euro excl. VAT)
E-mail address: _____

❖ Special Offer:
If you order 200 or more reprints you will get a PDF file for half price.

Please note: It is not permitted to present the PDF file on the internet or on company homepages.

Cover Posters (prices excl. VAT)

Posters of published covers are available in two sizes:

☐ DinA2 42 x 60 cm / 17 x 24in (one copy: 39 Euro)

☐ DinA1 60 x 84 cm / 24 x 33in (one copy: 49 Euro)

Postage for shipping (prices excl. VAT)
overseas +25 Euro
within Europe +15 Euro

_____
Date, Signature

VAT number: _____

Mail reprints to:
_____
_____
_____
_____
_____

Send bill to:
_____
_____
_____
_____

☐ **I will pay by bank transfer**

☐ **I will pay by credit card**

VISA, Mastercard and AMERICAN EXPRESS

For your security please use this link (Credit Card Token Generator) to create a secure code Credit Card Token and include this number in the form instead of the credit card data. Click here:
https://www.wiley-vch.de/editorial_production/index.php

CREDIT CARD TOKEN NUMBER

						V									

Wiley-VCH GmbH – A company of John Wiley & Sons, Inc. –
Location of the Company: Weinheim – Trade Register: Mannheim, HRB 736569
Managing Directors: Sabine Haag and Dr. Guido F. Herrmann

WILEY-VCH